MHD-test particles simulations of moderate CME and CIR-driven geomagnetic storms at solar minimum

Mary K. Hudson[1,2], Scot R. Elkington[3], Zhao Li[1], Maulik Patel[1,2], Kevin Pham[2], Alex Boyd[4] and Allison Jaynes[5]

[1] *Physics and Astronomy Dept. Dartmouth College, Hanover, NH, USA*
[2] *NCAR High Altitude Observatory, Boulder, CO, USA*
[3] *Laboratory for Atmospheric and Space Physics, University of Colorado Boulder, Boulder, CO, USA*
[4] *Space Sciences Department, The Aerospace Corporation, Chantilly, VA, USA*
[5] *Department of Physics & Astronomy, University of Iowa, Iowa City, IA, USA*

Corresponding author: first and last name (mary.k.hudson@dartmouth.edu)

Key Points:

- MHD-test particle simulations of CME- and CIR-driven storms during the 2019 solar minimum are compared
- Simulations reproduce magnetopause loss for the CME-shock event and increased Phase Space Density (PSD) for the CIR event
- Radial transport dominates the CME-shock event main phase while local heating is seen in Van Allen Probes PSD for the longer CIR event

Plain Language Summary

Outer zone radiation belt electron flux is highly variable and responds differently to different solar wind drivers. Coronal Mass Ejections (CMEs) which are common at Solar Maximum, when the sun is most active with sunspots every 11 years, create interplanetary shocks as they propagate towards earth. These shocks compress the dayside magnetosphere and can cause rapid loss of outer zone electrons. Ensuing geomagnetic storms which accompany shocks can repopulate the magnetosphere on a rapid timescale. At solar minimum, the focus of this study, low latitude coronal holes, which are regions of open solar magnetic field lines attached and corotating with the sun (Corotating Interaction Regions, CIRs), allow high speed solar wind to reach the earth and drive increases in outer zone electron flux over many days. Two geomagnetic storms during the 2019 Solar Minimum, one CME-driven and one CIR-driven, are investigated using a global model of the solar wind interaction with the magnetosphere and compared with measurements of electron flux from the twin Van Allen Probes spacecraft in the inner magnetosphere.

Abstract

As part of the Whole Heliosphere and Planetary Interactions (WHPI) initiative, contrasting drivers of radiation belt electron response at solar minimum have been investigated with MHD-test particle simulations for the 13 – 14 May 2019 CME-shock event and the 30 August – 3 September 2019 high speed solar wind interval. Both solar wind drivers produced moderate geomagnetic storms characterized by a minimum Dst = - 65 nT and - 52 nT, respectively, with the August - September event accompanied by prolonged substorm activity. The latter, with characteristic features of a CIR-driven storm, produced the hardest relativistic electron spectrum observed by Van Allen Probes during the last two years of the mission, ending in October 2019. MHD simulations were performed using both the Lyon-Fedder-Mobarry global MHD code and recently developed GAMERA model coupled to the Rice Convection Model, run with measured L1 solar wind input for both events studied, and coupled with test particle simulations, including an initial trapped and injected population. Initial electron phase space density (PSD) profiles used measurements from the Relativistic Electron Proton Telescope (REPT) and MagEIS energetic particle instruments on Van Allen Probes for test particle weighting and updating of the injected population at apogee. Results were compared directly with measurements and found to reproduce magnetopause loss for the CME-shock event and increased PSD for the CIR event. The two classes of events are contrasted for their impact on outer zone relativistic electrons near the end of Solar Cycle 24.

1 Introduction

The Whole Heliosphere and Planetary Interactions (WHPI), an international initiative focusing on the Solar Cycle 24 solar minimum (https://whpi.hao.ucar.edu/), follows upon the Whole Sun Month in 1996 and the Whole Heliosphere Interval in 2008 (Gibson et al., 2010; Hudson et al., 2012), aiming to understand the interconnected sun-heliospheric-planetary system at solar minimum when the sun's magnetic field configuration is less complex than at solar maximum. Despite the relative infrequency of Coronal Mass Ejections (CMEs) compared with solar maximum, there were a series of CMEs and ensuing Interplanetary Shocks (IS) observed in May 2019 from a solar active region that emerged a month earlier, providing an opportunity for comparison of the geoeffectiveness of CME-shocks with Corotating Interaction Regions (CIRs), more characteristic of solar minimum, in driving outer zone relativistic electron dynamics. CIRs recurrent with the solar rotation were seen throughout 2018 – 2019 and dominated radiation belt electron variability during this time. Measurements from the Van Allen Probes twin satellites launched 30 August 2012 into a near equatorial-plane orbit inside 5.8 earth radii (Mauk et al., 2013) were available throughout the declining phase of Solar Cycle 24, until mid-October 2019 when the Van Allen Probes mission ended.

High-energy electrons at geostationary orbit (L ~ 6.6) show a clear relationship between high-speed solar wind and subsequent relativistic electron enhancements (Paulikas and Blake, 1979; Baker et al., 1979). This suggests that magnetospheric substorm activity driven by high solar wind speed and enhanced convection of the dayside to nightside reconnected magnetic flux may play an important role in providing plasmasheet seed electrons with energy up to a few hundred keV which are transported to the inner magnetosphere (Baker et al., 1986). Subsequent studies using data from the Solar, Anomalous, and Magnetospheric Particle Explorer (SAMPEX) and Polar spacecraft confirmed that high-speed solar wind streams are effective in producing outer radiation belt electron flux enhancements (Baker et al., 1997; Kanekal et al., 1999). Using data from the Highly Elliptical Orbit (HEO) spacecraft, it was demonstrated that strong relativistic electron acceleration occurs throughout the entire outer zone when the solar wind has a strong southward interplanetary magnetic field (IMF) component (Blake et al., 1997).

This earlier work demonstrated that many geomagnetic storms produce relativistic electron flux enhancements at GEO (geostationary orbit), while other storms do not (Reeves et al., 2003; Summers et al., 2004; Hudson et al., 2008). Reeves et al. (2011) found that the relativistic electron-solar wind speed relationship is not a simple linear one as posed by Paulikas and Blake (1979). Li et al. (2011) examined 15 years of solar wind data and compared with GEO observations of MeV electron flux finding that high solar wind speeds are not necessary for MeV enhancements when strong southward IMF Bz is present. The separation between high speed solar wind in CIRs and extended periods of southward IMF Bz associated with CME-shock driven storms can explain these disparate statistical conclusions about solar wind drivers of geomagnetic storms and their effective enhancement of outer zone electrons.

Figure 1 shows electron flux vs. time and radial location from the Relativistic Electron Proton Telescope (REPT) on the Van Allen Probes (Baker et al., 2013) in three energy ranges from 1 January 2018 until the end of the mission. A CME-shock induced enhancement in flux at 1.8 and 4.2 MeV on 14 May 2019 is indicated which was accompanied by a Dst = -65 nT geomagnetic storm. The time axis is expanded in Supporting Information **Figure S1a,** showing that the enhancement was preceded by a dropout. Measured solar wind parameters at L1 for this event are shown in **Figure 2a** from NASA OMNIWeb. Recurrent CIRs which map to a coronal hole on the sun produced flux enhancements seen throughout summer 2019 in the lower energy channels of Figure 1. Recurring enhancement in radiation belt electron flux at the solar rotation period has long been measured at geosynchronous orbit (Reeves, 1998). The first enhancement in the 7.7 MeV channel since 7-8 September 2017 (not shown) was seen for the Aug – Sept CIR event (the time axis is expanded in **Figure S1b**). The 7.7 MeV enhancement at the beginning of September occurs over several days, as will be seen in closer examination of this high-speed stream event, similar to the CME-shock driven enhancement of lower energy flux 15-16 May following a flux dropout 14 May. It is typical of these two types of solar wind drivers of radiation belt flux changes that the CME-shock driven case produces a prompt change while the CIR case modifies radiation belt electrons over a period of days, accompanied by a longer interval of high solar wind velocity as seen in **Figure 2b**.

Previous work has shown that the dynamic outer zone electron radiation belt evolves differently during storms driven by the two drivers (e.g., Borovsky and Denton, 2006; Denton et al., 2006; Kataoka and Miyoshi, 2006; Yuan and Zong, 2012). A study by Shen et al. (2017) compared CME-shock and CIR-driven storm effects on outer zone electrons using Van Allen Probes measurements, and found that CIR-driven events cause stronger enhancements at higher L values while CME-shock driven storms have a greater effect at lower L values in a statistical sense. Their study of 28 CME-shock driven and 31 CIR events between March 2013 through July 2016 spanned the transition from dominance of CME-shock to CIR-driven storms in the Van Allen Probes data set, corresponding to the declining phase of Solar Cycle 24.

In the present study we focus on two cases at solar minimum. The CME-shock driven storm of 13-14 May 2019 was by no means the most dramatic example of the Solar Cycle 24 declining phase in terms of either the geomagnetic storm strength or radiation belt electron enhancement (Baker et al., 2019), but it serves to demonstrate distinct physical mechanisms which dominate this type of event as contrasted with the integral effect of the CIR interval in our second case studied, 30 August - 3 September 2019. In the next section we describe models used to simulate the time evolution of outer zone electrons from an initial radial profile taken directly from Van Allen Probes measurements. We then compare MHD-test particle simulations for the two events and show that the electron phase space density at fixed first invariant evolves over a longer time interval in the August-September case, while changes occur faster for the CME-shock driven case of 13-14 May 2019, consistent with observations. We examine the relative contribution of the initially trapped electrons vs. those transported earthward from the plasmasheet in both event studies. We conclude with discussion of how both types of events played a role in maintaining outer zone electron fluxes during the Solar Cycle 24 minimum.

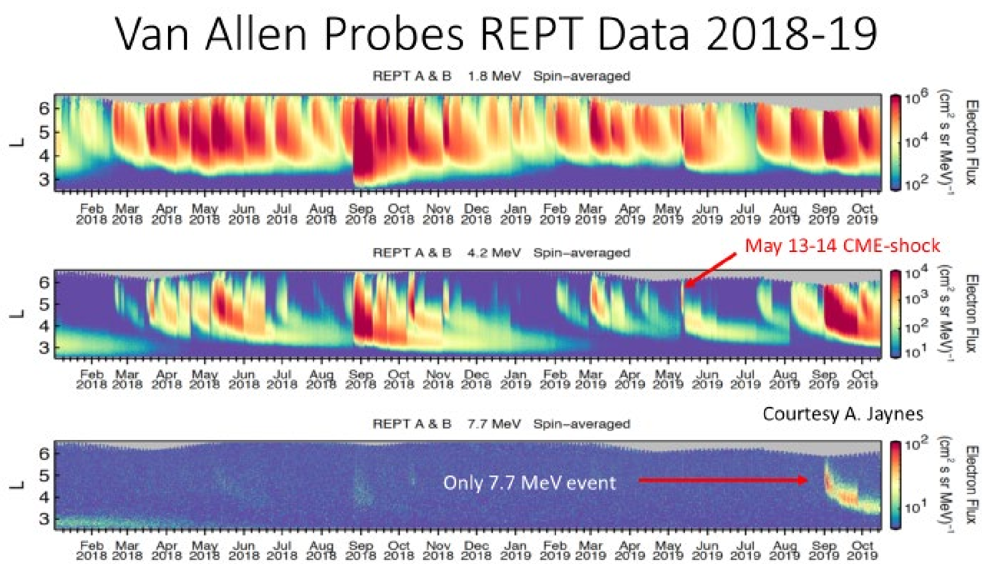

Figure 1. Differential electron flux vs. *L* value (vertical axis) and time (horizontal axis) from the Relativistic Electron Proton Telescope on Van Allen Probes (Baker et al., 2013) in three energy ranges from 1 January 2018 until the end of the mission. Arrows indicate the two event periods studied, a CME-shock event 13-14 May 2019 and a CIR event 30 Aug - 4 Sept 2019.

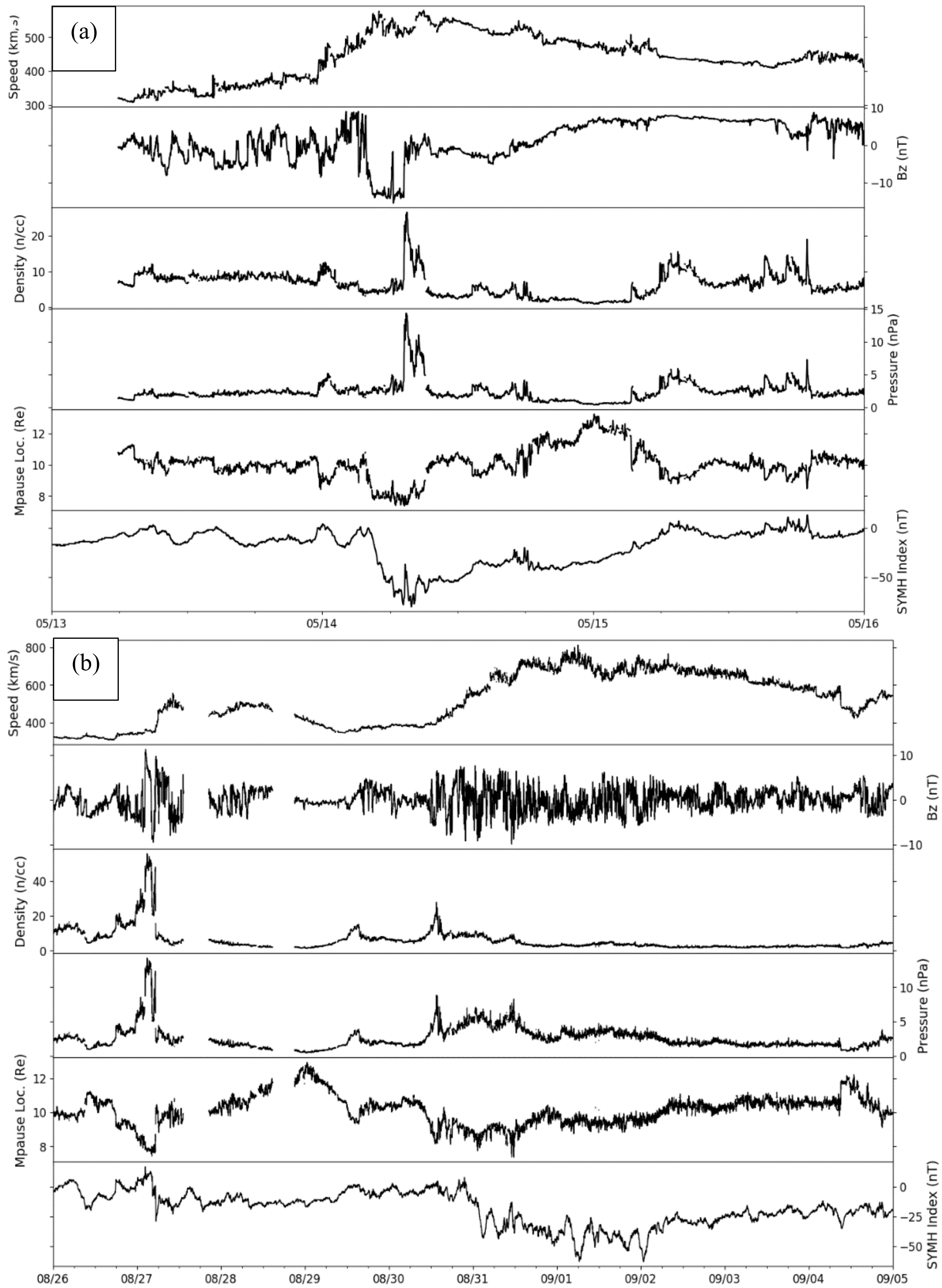

Figure 2. a) OMNIWeb solar wind data for 13 – 14 May 2019 CME-shock driven storm: speed Vsw, IMF Bz, density, pressure; Shue et al. (1998) magnetopause location and SymH in bottom two panels. CME-shock arrives at Earth ~ 00 UT 14 May. b) same for Aug-Sept 2019 CIR event. Vsw exceeds 600 km/s after 09 UT 31 Aug. The magnetopause location remains well outside geosynchronous for both events, however it is compressed inward to L = 8 for the CME-shock event. OMNIWeb time shift of L1 data to the noon bow shock is described at: https://omniweb.gsfc.nasa.gov/html/ow_data.html#time_shift

2 Models

We use global MHD and test particle modeling tools developed to simulate magnetospheric response to measured upstream solar wind input. We begin with the Lyon-Fedder-Mobarry model (Lyon et al., 2004) coupled to the Rice Convection Model (Pembroke et al., 2012; Wiltberger et al., 2015) to incorporate drift physics in the inner magnetosphere, with a Gallagher et al. (2000) Kp = 3 plasmasphere density weighting of the zeroeth energy channel of RCM to model a fixed plasmasphere. LFM fields were used in test particle simulations for the May CME-shock event while a parallel set of MHD simulations were run for the two events studied using the newer GAMERA MHD model which draws heritage from LFM, but has greater computational efficiency for longer runs (Zhang et al., 2019). The GAMERA model is again coupled to the Rice Convection Model, with the zeroeth energy channel of RCM initialized with a Kp = 2 plasmasphere profile (Gallagher et al., 2000), then allowed to evolve in the MHD fields with a fixed refilling rate (Pham et al., 2021). MHD input parameters for both event simulations were taken from OMNIWeb. The LFM model uses a computational domain extending from +30 Re to -300 Re along the sun-earth line (SM-x) and from -150 Re to +150 Re along SM-y and SM-z (–110 Re to + 110 Re for GAMERA along SM-y,z). All MHD input variables are assumed to be uniform in y and z at the upstream boundary. The LFM simulation grid has resolution 106 x 96 x 128 along radial, azimuthal and polar directions. The GAMERA grid resolution used is comparable. The inner boundary for LFM simulations is at 2 Re and for GAMERA is at 1.5 Re geocentric radius, with coupling to the ionosphere using an electrostatic potential solver incorporating changes in field-aligned currents and dynamic conductivities for both models (Merkin and Lyon, 2010). The MHD fields are dumped at 1min cadence.

For this project we use the 2D particle tracing code developed by Elkington et al. (2002) which follows the drift motion of guiding center electrons on a Cartesian grid in the MHD fields. Test particle electrons are initiated on the equatorial plane between 3 and 5.8 Re for the trapped population with a flat azimuthal distribution across all MLT for a total of 1 million test particles. As a post-processing step the test particles are weighted using the measured electron Phase Space Density (PSD) calculated at fixed first and second invariants from flux measured by the ECT instrument suite on Van Allen Probes (Spence et al., 2013), which includes high energies (> 2 MeV) measured by REPT and energies below 2 MeV measured by the MagEIS instrument (Blake et al., 2013). The weighting algorithm uses the orbit prior to the beginning of each test particle simulation to serve as an initial radial profile. The injected population is launched continuously from an annulus sector which spans 165 – 195 degrees from noon centered on midnight with a radial location of 5.8 – 6 Re. The PSD in the annulus is updated in the simulations at the value corresponding to the measured PSD at apogee from Van Allen Probes, which takes into account increased PSD due to plasmasheet injections and any local heating that increases PSD beyond the apogee of the Van Allen Probes (Boyd et al., 2018). The first invariant is chosen to be 2000 MeV/G and 5000 MeV/G to cover the energy ranges shown in Figure 1 in the inner magnetosphere. Both May and Aug - Sept events have 1 million trapped particles initially. Test particles representing a plasmasheet source are injected at 70,000/hr, randomly distributed in the 5.8 – 6 Re, 30 degree anulus centered on midnight shown in Figure 3. Both populations are weighted in a post-processing step with the same methods from Nunn (1993) so as to conserve PSD according to Liouville's theorem.

3 Results for May 13-14 CME-shock driven geomagnetic storm

Figure 2a shows OMNIWeb solar wind parameters used as input to MHD test particle simulations of the May 13 – 14 CME shock event along with the magnetopause location from the Shue et al. (1998) model and SymH, which indicates changes in magnetospheric current systems, primarily the ring current. The disturbance arrival at L1 is at 2326 UT in the Cane and Richardson list of ICMEs (http://www.srl.caltech.edu/ACE/ASC/DATA/level3/icmetable2.htm) while the OMNIWeb data shown in Figure 2a is propagated to the bow shock nose assuming purely radial propagation in GSE coordinates at the measured solar wind velocity. Solar wind velocity, density and pressure increase around 00 UT on 14 May in Figure 2a with southward turning of IMF Bz around 04 UT driving buildup of the ring current and a SymH minimum. **Figure 3a** shows the initial configuration of the GAMERA simulations (LFM is comparable, and Bz from the two models is compared in **Figure S6** at 0530 UT 14 May), including dipole tilt evident in the meridional plot of MHD pressure on the right, with northern and southern hemispheric field aligned currents in the polar regions shown as inserts. On the left, residual Bz (dipole subtracted) is plotted along with an insert showing RCM pressure in the inner magnetosphere**.** The LFM simulation was run from 2100 UT on 13 May to 1000 UT on 14 May. Test particle simulations were begun at 2300 UT on 13 May for a total run time of 11 hours to capture the rapid CME-shock impact effects on the magnetosphere. A longer multiday simulation was run for the Aug-Sept CIR event. **Figure 3b** shows the initial location of test particles traced in the MHD fields, with the initial trapped population in black and injected electrons in red.

Figure 4 shows the Phase Space Density profile for 2000 MeV/G electrons measured by the ECT instrument on the Van Allen Probes used for initial test particle weighting in the simulation studies, beginning with blue curves shown at 00 UT on 13 May and 00 UT on 29 August, respectively, with subsequent orbits indicated by the color bar on the right over the next 2 days. The black curve indicates the PSD profile used for weighting the trapped test particle population chosen to reflect the initial radial profile for each event, e.g. prior to the interplanetary shock for the May event. Note 1) that initial PSD is a factor 100 times higher for the May case and 2) flat at higher L, while increasing at higher L for the Aug-Sept case. An assumption must be made about assigning phase space density to test particles, which is then conserved according to Liouville's Theorem. McCollough et al. (2009) implement the areal weighting scheme of Nunn (1993), used here in the 2D test particle simulations. Here PSD is plotted vs. L* (Roederer, 1970) using the TS04 magnetic field model (Tsyganenko and Sitnov, 2005), which is inversely proportional to flux inside an electron drift orbit adiabatically conserved in the absence of field variations on the electron drift time.

(a)

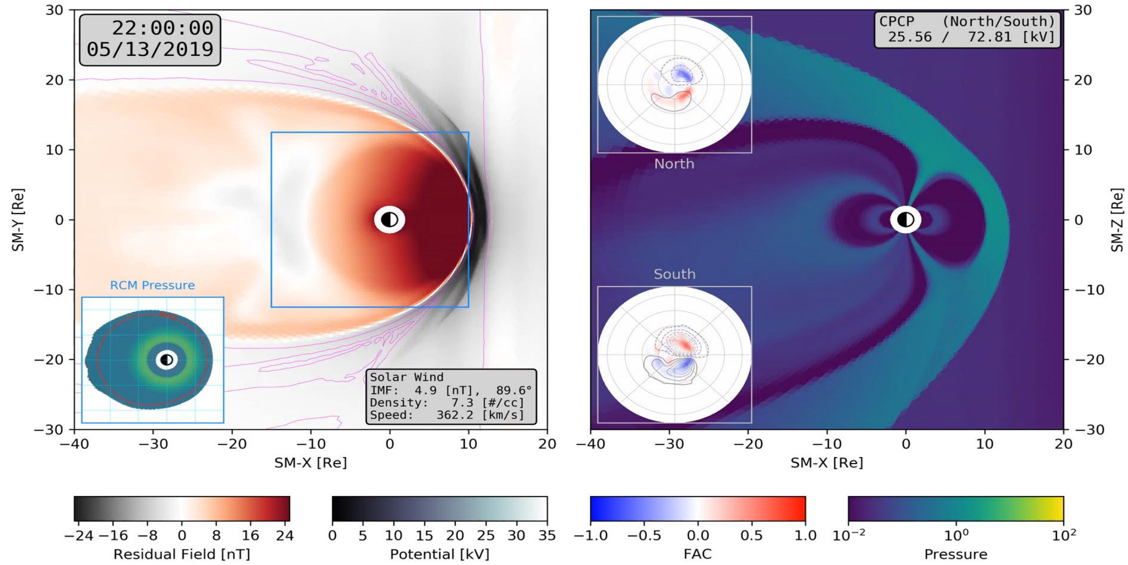

(b)

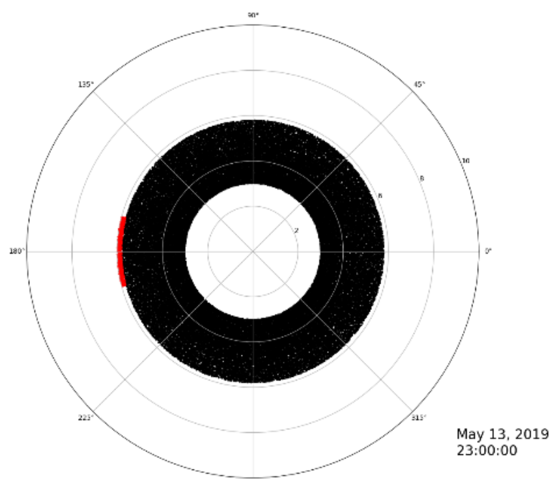

Figure 3. a) CME-shock simulation shown at 2200 UT 13 May 2019, using GAMERA 3D MHD code coupled to the Rice Convection Model and TIEGCM ionospheric model (Pham et al., 2021). Meridional plot of MHD pressure is shown on the right, with northern and southern hemispheric field aligned currents in the polar regions shown as inserts. On the left, residual Bz (dipole subtracted) is plotted along with an insert showing RCM pressure in the inner magnetosphere**.** Upstream solar wind input is taken from OMNIWeb (Figure 2) propagated to the 30 Re upstream boundary. b) Initial test particle populations in the GSM equatorial plane. Injected (red) and trapped (black) are the same for both May and Aug – Sept 2019 event studies prior to weighting with PSD measured from Van Allen Probes.

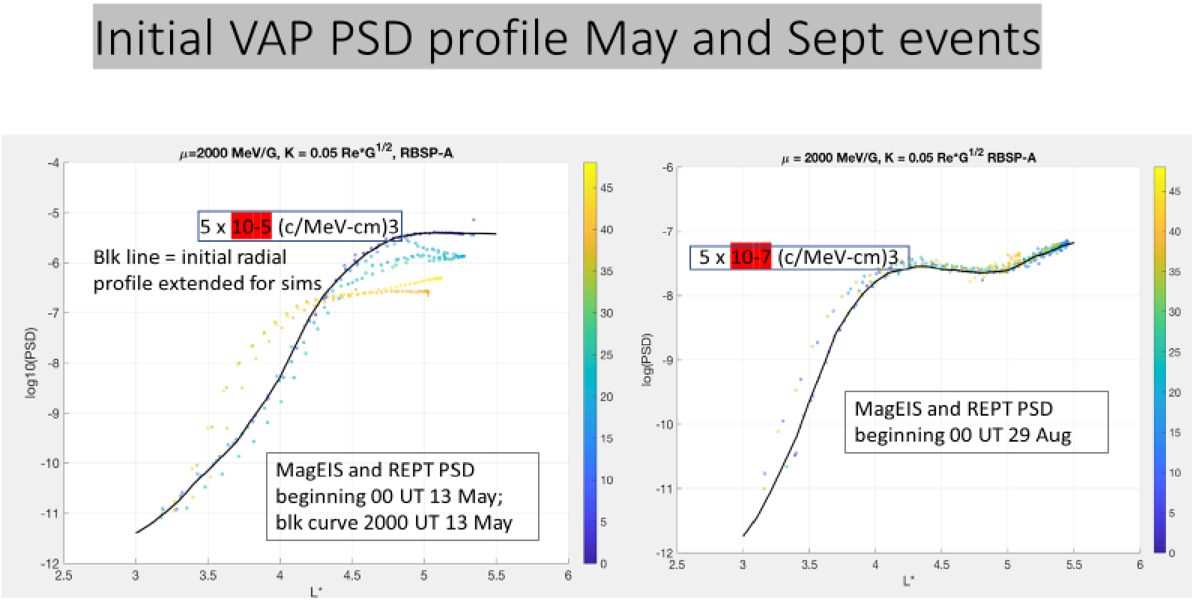

Figure 4. Radial profile of PSD for protons measured by REPT and MagEIS instruments on Van Allen Probe A for first invariant M = 2000 MeV/G (2 MeV at L = 6.6 in a dipole) and second invariant K =0.051 Re $G^{0.5}$ plotted vs. L* (Roederer, 1970) using the TS04D magnetic field model (Tsyganenko and Sitnov, 2005). Initial orbit is shown (blue) and subsequent orbits indicated over 48 hours from 0 UT 13 May (left) and 0 UT 29 Aug (right). Black curve is used for simulated initial PSD radial profile of the trapped population for each event.

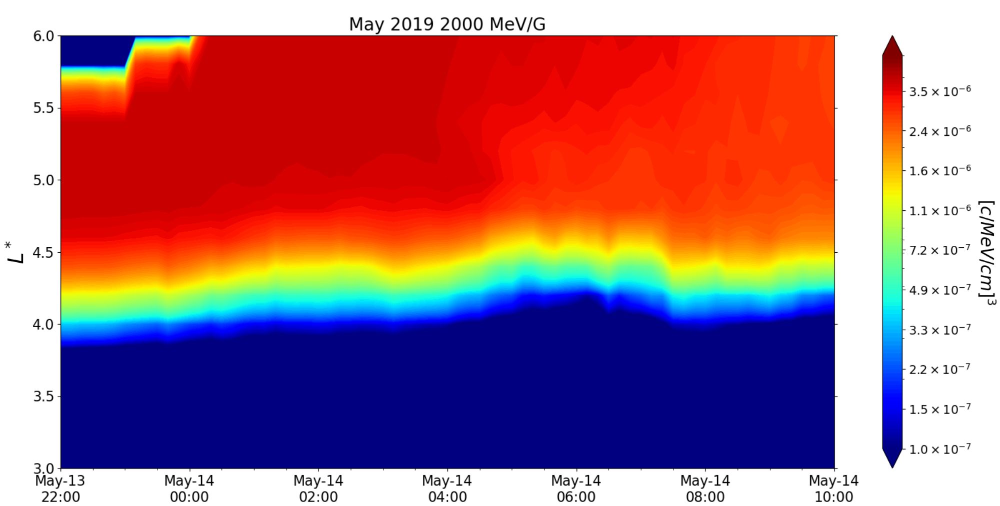

Figure 5. Simulated PSD (trapped + injected) radial profile vs. L* following arrival of IP shock at L1 at 23:26 UT 13 May is shown. IMF Bz reaches a southward minimum at 06 UT 14 May and min Dst = -65 nT at 08 UT (http://wdc.kugi.kyoto-u.ac.jp/dst_realtime/201905/index.html), see Fig. 2a. The blue patch of low PSD in the upper left corner is due to mapping from L to L* since test particles are initialized inside L = 6 Re, see Figure 3b, which is inside L* = 6 Re using the TS04D magnetic field model for mapping.

Figure 5 shows simulated PSD using LFM-RCM fields to advance test particles, updating the outer boundary test particle weighting of injected electrons with measured PSD at apogee (r = 5.8 Re) every 9 hours for each spacecraft. The initial measured radial profile from Van Allen Probes plotted as the black curve in Figure 5a is used to initialize the radial weighting profile of the trapped population, while the plasmasheet population is injected between r = 5.8 and 6 Re in a 30 degree anulus with PSD weighting that matches the measured PSD at apogee, see Figure 3b. Strong erosion of the dayside magnetopause which coincides with southward turning of IMF Bz, seen in the Shue et al. (1998) model magnetopause plotted in Figure 2a beginning around 04 UT on 14 May, drives magnetopause loss over the 11 hour simulation time scale shown in Figure 5. L is mapped into L* using the LANLstar artificial neural network trained using the TS04D magnetic field model (https://spacepy.github.io/lanlstar.html). The 10 min time-varying solar wind parameters and TS04D coefficients were obtained from Tsyganenko's database archive (https://geo.phys.spbu.ru/~tsyganenko/TS05_data_and_stuff/). Dst reaches a minimum around 08 UT and adiabatic relaxation of the magnetic field during recovery phase (Kim and Chan, 1997) contributes to inward radial transport. However, mapping PSD in L* (within uncertainties of the L-L* mapping algorithm) should remove dominance of adiabatic relaxation, so inward radial transport seen in Figure 5 suggests that radial diffusion is occurring, as seen and modeled in other CME-shock driven storms (see Li et al., 2017 and references). The PSD plot combines contributions from plasmasheet injection with the initial trapped population. As seen in Supporting Information **Figure S3**, the trapped population makes a larger contribution at lower L* values than the injected population by the end of the 11-hour simulation. We will find the opposite behavior for the long duration simulation of the Aug-Sept CIR event, where the contribution from plasmasheet injection dominates. Results for 5000 MeV/G are shown in **Figure S5.**

Figure 6 shows the evolution of PSD for the Aug - Sept event for 2000 MeV/G electrons using GAMERA fields. The test particle simulations are run longer for the Aug – Sept event (00 UT 30 Aug to 00 UT 3 Sept) to capture the time interval of CIR driving of outer zone electron response in contrast with the CME-shock event study (11 hours) which evolves faster. Kp reached a maximum of 6 on both 31 Aug and 1 Sept (not shown), indicating strong substorm activity on those days. Ten substorms occurred during the time interval simulated, see Supporting Information Table S1. The contributions of the injected and initial trapped population are plotted separately in **Figure S4.** Here the injected population dominates over the course of the CIR-driven storm with a more slowly evolving ring current than for the CME-shock driven storm (contrast SymH in the bottom panels of Figures 2a and 2b). While loss to the magnetopause is a prominent feature for the CME-shock driven case, the CIR-driven storm is characterized by emergence of a local peak in PSD associated with updating the PSD carried by injected test particles at the Van Allen Probe A apogee every 9 hours (Van Allen Probe B ceased operations 19 July 2019), spreading to higher and lower L* through radial transport. Figures 5 and 6 provide a stark contrast between the two types of events studied which will next be compared directly with measured PSD.

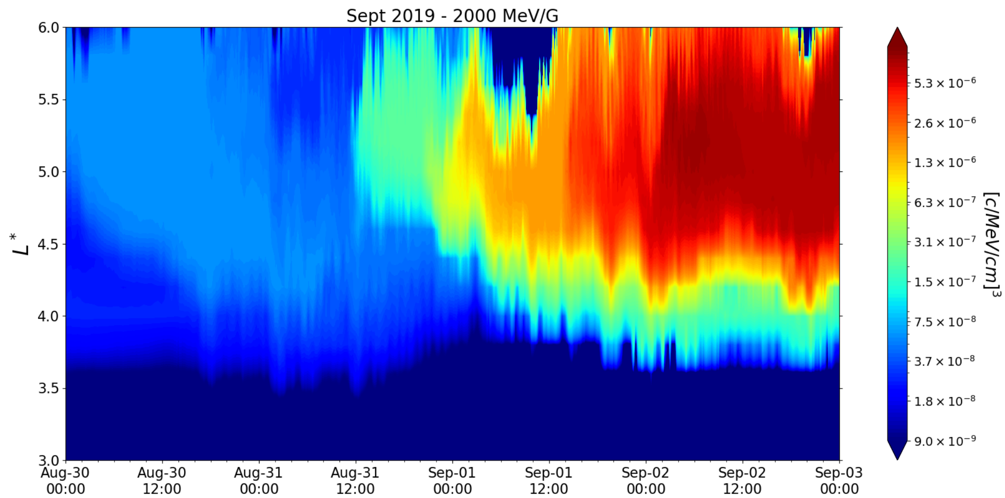

Figure 6. Simulated PSD (trapped + injected) radial profile vs. L* using TS04 model during the CIR interval shown in Fig. 2b. Vsw exceeds 600 km/s after 09 UT 31 Aug, IMF Bz is oscillatory around 0 nT with min Dst = - 52 nT at 07 UT on 1 Sept in Fig. 1b. Test particle simulation was started at 00 UT 30 Aug and ran until 0900 UT on 2 Sept.

Figure 7 (top panels) compares the measured PSD at 2000 and 5000 MeV/G for the May CME-shock event over 48 hours starting at 0 UT 13 May with the simulated PSD at 34 hours (10 UT 14 May) shown in black dots. The initial orbit of measured PSD is shown in dark blue and subsequent orbits of the two Van Allen Probes spacecraft are indicated over 2 days from 0 UT 13 May to 0 UT 15 May shown in yellow. Black dots indicate the radial profile at the end of the simulation shown in Figure 5. Inward radial transport relative to the initial radial profile is evident in both simulated and measured PSD. Loss at higher L is captured for both first invariants (compare black dots with green at 34 hours). Atmospheric loss processes produced by higher frequency whistler mode or EMIC waves are not included in the MHD simulations (see review by Li and Hudson, 2019). However, the decrease in PSD at higher L values is consistent with magnetopause loss seen in other MHD-test particle simulations where loss due to radial transport and inward motion of the magnetopause dominates (Hudson et al., 2014). Decrease in PSD at higher L is greater at 5000 MeV/G than at 2000 MeV/G, consistent with the shorter timestep for a random walk in the radial variable (radial diffusion) as the drift period decreases with higher first invariant.

Figure 7 (bottom panels) compares the measured PSD at 2000 and 5000 MeV/G for the Aug-Sept CIR-driven event. Note that the timescale for the CIR event shown is 4 days vs. 2 days for the CME-shock event comparison, since the evolution occurs over a longer timescale for CIR driving than for CME-shocks producing more abrupt changes, in particular magnetopause loss (Hudson et al., 2014; 2015). While the CME-shock event produced a loss of PSD over the timescale shown, the CIR event produced a substantial increase in PSD over three orders of magnitude at 2000 and 5000 MeV/G. There is good agreement between simulated and measured PSD at high and low L*, however the simulation does not capture the peak in PSD evident by 0

UT 3 September (yellow), likely due to local heating not included in the simulations (Boyd et al. 2018; see review by Li and Hudson, 2019).

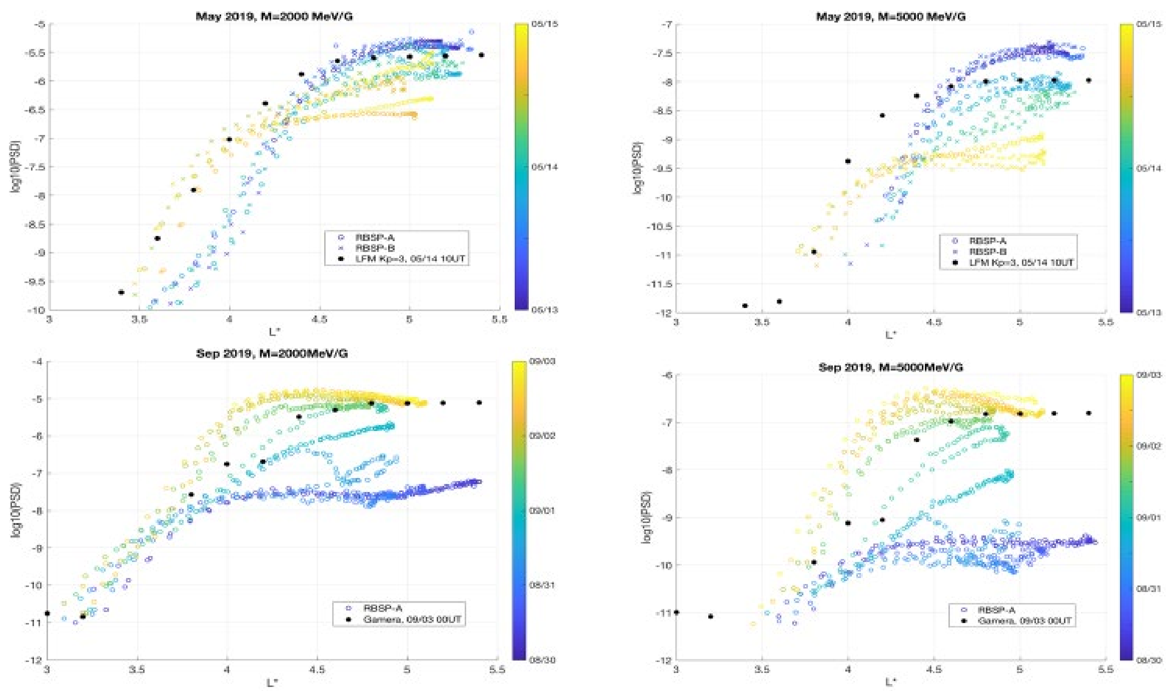

Figure 7. Comparison of simulated PSD radial profile at the end of the time intervals shown in Figures 5 and 6 (black dots) with measured PSD profiles from Van Allen Probes over sequential orbits. Initial orbit is shown (blue) and subsequent orbits are indicated over 2 days from 0 UT 13 May (top) and 4 days from 0 UT 30 Aug (bottom). Black dots indicate end of the simulation (after 34 hours of data shown for the May event and at 0 UT on 3 Sept for the September event) using PSD updated at apogee every 9 hours for the RBSPA and RBSP B spacecraft as available, with data combined for the May event and only RBSP A measurements available every 9 hours for the September event.

4 Discussion and Conclusions

In contrasting the two events studied, the CME-shock produced solar wind drivers characterized by a moderate solar wind pressure impulse at 00 UT on 14 May in Figure 2a and increase in solar wind velocity from 300 to 500 km/s, with IMF Bz turning southward to – 13 nT for 4 hours, and increased magnetospheric convection during this time building up the ring current as reflected in SymH. A second stronger pressure impulse occurred as Bz increased sharply around 07 UT on 14 May and is reflected in SymH. Otherwise, this event has characteristic solar wind driving features seen in other CME-shock driven storms which are distinct from the features seen in the Aug-Sept CIR event in Figure 2b. The CIR event is characterized by ~ 4 days of high solar wind velocity exceeding 600 km/s and a long but very moderate enhancement of the ring current reflected in SymH, beginning 00 UT 31 Aug and extending over a week, typical of CIR driven storms (Tsurutani et al., 2006). Embedded in this period of enhanced solar wind velocity characteristic of CIRs, Alfvenic fluctuations typically drive recurring substorms, providing a seed population for radiation belt electron enhancement when plasmasheet electrons are efficiently transported earthward via enhanced convection and dipolarization events (Borovsky and Denton, 2006). **Table S1** in the Supporting Information provides a list of substorms during the CIR event. Five substorms occurred on 30 August, just prior to the drop in SymH, with subsequent days of multiple substorm occurrence (2 and 3 September). Kp reached an event high of 6 on 31 Aug and 1 Sept (not shown).

These contrasting scenarios of solar wind driving for the CME-shock and CIR events explain the different timescales for PSD evolution seen in the two cases. The CME-shock event initiated by an L1 disturbance at 2326 UT on 13 May was followed by another CME-shock at 2100 UT on 16 May, the third and fourth of five ICME shocks in the Cane- Richardson ICME shock list for May 2019, and the only ICME shocks arriving at L1 between 23 Sept 2018 and 29 Oct 2019 (http://www.srl.caltech.edu/ACE/ASC/DATA/level3/icmetable2.htm), all five from the same active region on the sun. The 13-14 May event caused initial loss from inward motion of the magnetopause, characteristic of CME-shock driven storms (Hudson et al., 2014; 2015). We focused on the dropout period for the May event since recovery likely involves local heating by whistler mode chorus not contained in the MHD-test particle model (Thorne et al., 2013). Outer zone electron dropout events are a common feature of geomagnetic storms at higher L shells (e.g., Green et al., 2004; Matsumura et al., 2011; Millan and Thorne, 2007; Morley et al., 2010; Ni et al., 2013; Onsager et al., 2002; Shprits et al., 2006; Su et al., 2017; Turner et al., 2012; Turner et al., 2014a; Turner et al., 2014b; Ukhorskiy et al., 2015; Xiang et al., 2017). Rapid radial loss is observed with CME shock-driven storms (Hudson et al., 2014) and well correlated with the last closed drift shell during strong magnetopause compression (Albert et al., 2018; Olifer et al., 2018). Drift shell splitting is enhanced during such events with electrons near 90° pitch angle moving to larger radial distance on the dayside conserving their first adiabatic invariant (Roederer, 1967, 1970). They may then be preferentially lost to the magnetopause. Fast inward motion of the magnetopause can produce a negative PSD gradient which leads to outward radial diffusion (e.g., Shprits et al., 2006), particularly in the presence of enhanced ULF wave power which follows such compressions (e.g., Hudson et al., 2014, 2015; Zong et al., 2009; Zong et al., 2017). The Dst effect (Kim and Chan, 1997) is weak for the moderate storms in the present study, however calculating PSD from measured and simulated flux using a model magnetic field (TS04D) allows for inclusion of adiabatic reduction in flux due to buildup of the ring current and outward motion of electrons conserving their magnetic flux through a drift orbit, the third adiabatic invariant. The local magnetic field is weakened by the opposing magnetic field due to the ring current (Kim and Chan, 1997).

The Aug – Sept CIR driven storm was weaker and the initial PSD at 2000 MeV/G was lower by two orders of magnitude as seen in Figure 4 relative to the CME-shock event. Nonetheless, a strong enhancement is seen both at 2000 and 5000 MeV/G for the Aug – Sept event, see Figure 7 bottom, with a three order of magnitude enhancement in PSD at 2000 and 5000 MeV/G. Note that the flux enhancement occurs first at lower energies, at 1.8 then at 4.2 MeV in Figure 1, before enhancement is seen at 7.7 MeV. This delayed enhancement at higher energies is commonly observed and expected both for energization due to inward radial transport conserving the first invariant and for local acceleration by whistler mode chorus, a process which is expected during recurring substorms.

Jaynes at al. (2015) have identified two distinct electron populations resulting from magnetospheric substorm activity which are crucial for the acceleration of highly relativistic electrons in the outer zone: a *source* population (tens of keV) that gives rise to whistler mode chorus growth and a *seed* population (hundreds of keV) that is accelerated via interaction with the chorus to much higher energies (Thorne et al., 2013). By updating the simulations with measured PSD at the Van Allen Probes apogee, we effectively capture the enhanced seed population transported from the plasmasheet; however additional local acceleration and atmospheric loss due to higher frequency waves than captured by MHD physics (higher than the ion gyrofrequency) are not included in our simulations. The importance of these processes is expected to be greater over the longer timescale of a CIR event. However, the overall radial profile evolution of both events is well captured, with loss of the initial trapped population dominating the CME-shock driven storm during main phase and increase in PSD due to the injected population dominating the CIR-driven storm. MHD-test particle simulations have also captured well CME-shock driven prompt injection events such as 17 March 2015 (Hudson et al., 2017) and 16 July 2017 (Patel et al., 2019), wherein a stronger CME-shock produces a coherent magnetosonic wave disturbance inside the magnetosphere with an azimuthal electric field transporting trapped MeV electrons inward ahead of the magnetopause compression (Li et al., 1993; Hudson et al., 2020 reviews this type of event). For the weaker CME-shock event studied 13 – 14 May 2019, magnetopause loss is the dominant early signature of the event with no evidence of prompt injection in the REPT data. Later recovery over 15-16 May, shown in greater detail than Figure 1 in Figure S1, may be due to a combination of local heating by VLF waves and inward radial transport to which ULF waves contribute (see Li and Hudson, 2019 for a review of both processes).

Overall our conclusions in comparing the impact on outer zone electrons of a moderate CME-shock driven storm with a 4-day CIR event, more characteristic of solar minimum, supports our earlier conclusions about these two distinct types of solar wind drivers based on separate studies (Hudson et al., 2012; Hudson et al., 2014; 2015). Here we use well-developed MHD-test particle tools with input parameters calibrated to measured PSD at 5.8 Re to study both events. Increased MHD grid resolution and coupling to RCM significantly advances our prior 4-day CIR study for the Whole Heliosphere Interval at the last solar minimum (Hudson et al., 2012), bringing code resolution and representation of the ring current up to the level of recent work on CME-shock driven storms during the Van Allen Probes era. Future work will make further quantitative comparisons using the newly developed GAMERA code which allows for longer simulation studies at higher efficiency (Zhang et al., 2019; Pham et al., 2021). It remains for us to add a model for the atmospheric losses which accumulate over longer runs like the Aug – Sept CIR event.

Acknowledgments

This study is supported by NASA grant 80NSSC17K0678 and JHU/APL under NASA contracts NNN16AA09T and NNN06AA01C and NASA DRIVE Science Center for Geospace Storms (CGS) under grant 80NSSC20K0601. We acknowledge high-performance computing support from NCAR CISL.

Data Availability Statement

Solar wind data can be accessed at https://omniweb.gsfc.nasa.gov. Van Allen Probe REPT/ECT data can be accessed at the website (https://www.rbsp-ect.lanl.gov). The simulation data used to create the figures are available via Zenodo website (https://doi.org/10.5281/zenodo.5163030).

References

Albert, J. M., Selesnick, R. S., Morley, S. K., Henderson, M. G., & Kellerman, A. C. (2018). Calculation of last closed drift shells for the 2013 GEM radiation belt challenge events. *Journal of Geophysical Research: Space Physics,* 123, 9597–9611. https://doi.org/10.1029/ 2018JA025991**.**

Baker, D. N., P. R. Higbie, R. D. Belian, and E. W. Hones Jr. (1979), Do Jovian electrons influence the terrestrial outer radiation zone?, *Geophys. Res. Lett.*, 6, 531– 534, doi:10.1029/GL006i006p00531.

Baker, D. N., J. B. Blake, R. W. Klebesadel, and P. R. Higbie (1986), Highly relativistic electrons in the Earth's outer magnetosphere, I. Lifetimes and temporal history 1979–1984, *J. Geophys. Res.*, 91, 4265– 4276, doi:10.1029/JA091iA04p04265.

Baker, D. N., et al. (1997), Recurrent geomagnetic storms and relativistic electron enhancements in the outer magnetosphere: ISTP coordinated measurements, *J. Geophys. Res.*, 102, 14,141– 14,148, doi:10.1029/97JA00565.

Baker, D. N., et al. (2013), The Relativistic Electron-Proton Telescope (REPT) Instrument on Board the Radiation Belt Storm Probes (RBSP) Spacecraft: Characterization of Earth's Radiation Belt High-Energy Particle Populations, *Space Sci. Rev.*, 179, 337– 381, doi:10.1007/s11214-012-9950-9.

Baker, D. N., Hoxie, V., Zhao, H., Jaynes, A. N., Kanekal, S., Li, X., & Elkington, S. (2019). Multiyear measurements of radiation belt electrons: Acceleration, transport, and loss. *Journal of Geophysical Research: Space Physics*, 124, 2588– 2602. https://doi.org/10.1029/2018JA026259.

Blake, J. B., D. N. Baker, N. Turner, K. W. Ogilvie, and R. P. Lepping (1997), Correlation of changes in the outer-zone relativistic electron population with upstream solar wind and magnetic field measurements, *Geophys. Res. Lett.*, 24, 927– 929, doi:10.1029/97GL00859.

Blake, J., et al. (2013), The Magnetic Electron Ion Spectrometer (MagEIS) instruments aboard the Radiation Belt Storm Probes (RBSP) spacecraft. *Space Science Reviews*, 179, doi: 10.1007/s11214-012-9950-9.

Borovsky, J. E. and M. H. Denton, 2006, Differences between CME‐driven storms and CIR‐driven storms, *J. Geophys. Res., 111*, A07S08, doi:10.1029/2005JA011447.

Boyd, A. J., Turner, D. L., Reeves, G. D., Spence, H. E., Baker, D. N., & Blake, J. B. (2018). What causes radiation belt enhancements: A survey of the Van Allen Probes Era. *Geophysical Research Letters*, 45, 5253– 5259. https://doi.org/10.1029/2018GL077699.

Denton, M., J. Borovsky, R. Skoug, M. Thomsen, B. Lavraud, M. Henderson, M. RL, J. Zhang, and M. Liemohn (2006), Geomagnetic storms driven by ICME- and CIR-dominated solar wind, *J. Geophys. Res.*, 111, A07S07 doi:10.1029/2005JA011436.

Elkington, S., Hudson, M., Wiltberger, M., & Lyon, J. (2002). MHD/particle simulations of radiation belt dynamics. *Journal of Atmospheric and Solar-Terrestrial Physics*, 64, 233.

Elkington, S.R., M. Wiltberger, A.A. Chan, and D.N. Baker, 2004, Physical Models of the Geospace Radiation Environment, *J. Atmos. Solar-Terr. Phys.,* 66/15-16, 1371.

Gallagher, D. L., P. D. Craven, and R. H. Comfort (2000), Global core plasma model, *J. Geophys. Res.,* 105, 18,819–18,833, doi:10.1029/1999JA000241.

Gibson, S. E., Webb, D. F., and Thompson, B. J., 2010, The Whole Heliosphere Interval in the context of the current solar minimum, Proceedings of SOHO 23 workshop, ASP Conference Series, Volume 428, Steven Cranmer, Todd Hoeksema, and John Kohl, eds., 223.

Green, J. C., & Kivelson, M. G. (2004). Relativistic electrons in the outer radiation belt: Differentiating between acceleration mechanisms. *Journal of Geophysical Research*, 109, A03213. https://doi.org/10.1029/2003JA010153.

Hudson, M. K., B. T. Kress, H.-R. Mueller, J. A. Zastrow and J. B. Blake (2008), Relationship of the Van Allen radiation belts to solar wind drivers, invited review, *J. Atmos. And Solar. Terr. Phys.,* Vol 70/5 pp 708-729, 10.1016/j.jastp.2007.11.003.

Hudson, M.K., T. Brito, S. Elkington, B. Kress, Z. Li and M. Wiltberger (2012), Radiation belt 2D and 3D simulations for CIR-driven storms during Carrington Rotation 2068, *J. Atmos. Solar Terres. Phys., 83, p. 51-62.*

Hudson, M. K., D. N. Baker, J. Goldstein, B. T. Kress, J. Paral, F. Toffoletto, and M. Wiltburger (2014), Simulated magnetopause losses and Van Allen Probe flux dropouts, *Geophysical Research Letters,* doi:10.1002/2014gl059222.

Hudson, M. K., J. Paral, B. T. Kress, M. Wiltburger, D. N. Baker, J. C. Foster, D. L. Turner, and J. R. Wygant (2015), Modeling CME-shock driven storms in 2012-2013: MHD-test particle simulations, *J. Geophys. Res.*, doi:10.1002/2014JA020833.

Hudson, M. K., A.N Jaynes, B.T. Kress, Z. Li, M. Patel, X.-C. Shen, S.A. Thaller, M. Wiltberger, *and* J. Wygant (2017), Simulated prompt acceleration of multi-MeV electrons by the 17 March 2015 interplanetary shock, *J. Geophys. Res*., 122, *doi:*10.1002/2017JA024445.

Hudson, M. K., M. Patel, S. Elkington, Z. Li, B. Kress, K. Pham, MHD-test particles simulations of moderate CME and CIR-driven geomagnetic storms at solar minimum and comparison with Van Allen Probes radiation belt electron measurements (2020), Fall AGU Meeting.

Jaynes, A. N., et al. (2015), Source and seed populations for relativistic electrons: Their roles in radiation belt changes, *J. Geophys. Res. Space Physics*, 120, 7240– 7254, doi:10.1002/2015JA021234.

Jaynes, A. N., Ali, A. F., Elkington, S. R., Malaspina, D. M., Baker, D. N., Li, X., et al. (2018). Fast diffusion of ultrarelativistic electrons in the outer radiation belt: 17 March 2015 storm event. *Geophysical Research Letters*, 45, 10,874– 10,882. https://doi.org/10.1029/2018GL079786

Kanekal, S. G., D. N. Baker, J. B. Blake, B. Klecker, R. A. Mewaldt, and G. M. Mason (1999), Magnetospheric response to magnetic cloud (coronal mass ejection) events: Relativistic electron observations from SAMPEX and Polar, *J. Geophys. Res.*, 104(A11), 24,885– 24,894, doi:10.1029/1999JA900239.

Kataoka, R., and Y. Miyoshi (2006), Flux enhancement of radiation belt electrons during geomagnetic storms driven by coronal mass ejections and corotating interaction regions, *Space Weather*, 4, S09004, doi:10.1029/2005SW000211.

Kim, H.-J., and Chan, A. A. (1997), Fully adiabatic changes in storm time relativistic electron fluxes, *J. Geophys. Res.*, 102(A10), 22107– 22116, doi:10.1029/97JA01814.

Li, X., Roth, I., Temerin, M., Wygant, J.R., Hudson, M.K., Blake, J.B., 1993. Simulation of the prompt energization and transport of radiation belt particles during the March 24, 1991 SSC. *Geophys. Res. Lett.* 20 (22), 2423–2426.

Li, X., M. Temerin, D. N. Baker, and G. D. Reeves (2011), Behavior of MeV electrons at geosynchronous orbit during last two solar cycles, *J. Geophys. Res.*, 116, A11207, doi:10.1029/2011JA016934.

Li, Zhao, M. Hudson, B. Kress, and J. Paral (2015), Three-dimensional test particle simulation of the 17-18 March 2013 CME shock-driven storm, *Geophysical Research Letters, 42,* 14, doi:10.1002/2015gl064627.

Lyon, J., J. Fedder, and C. Mobarry (2004), The Lyon-Fedder-Mobarry (LFM) global MHD magnetospheric simulation code, *J. Atmos. Sol. Terr. Phys.*, 66(15-16), 1333– 1350, doi:10.1016/j.jastp.2004.03.020.

Matsumura, C., Miyoshi, Y., Seki, K., Saito, S., Angelopoulos, V., & Koller, J. (2011). Outer radiation belt boundary location relative to the magnetopause: Implications for magnetopause shadowing. *Journal of Geophysical Research*, 116, A06212. https://doi.org/10.1029/2011JA016575.

Mauk, B., Fox, N. J., Kanekal, S., Kessel, R., Sibeck, D., & Ukhorskiy, A. (2013). Science objectives and rationale for the radiation belt storm probes mission. *Space Science Reviews,* 179, 3–27. https://doi.org/10.1007/s11214‐012‐9908‐y.

McCollough, J. P., J. L. Gannon, D. N. Baker, and M. Gehmeyr (2008), A statistical comparison of commonly used external magnetic field models, *Space Weather*,6, S10001, doi:10.1029/2008SW000391.

McCollough, J. P., S. R. Elkington, and D. N. Baker, 2009, Modeling EMIC wave growth during the compression event of 29 June 2007, *Geophys. Res. Lett., 36*, L18108, doi:10.1029/2009GL039985.

Merkin, V. G., and Lyon, J. G. (2010), Effects of the low-latitude ionospheric boundary condition on the global magnetosphere, *J. Geophys. Res.*, 115, A10202, doi:10.1029/2010JA015461.

Millan, R. M., and Thorne, R. M. (2007). Review of radiation belt relativistic electron loss. *Journal of Atmospheric and Solar - Terrestrial Physics, 69*, 362–377. https://doi.org/10.1016/j.jastp.2006.06.019.

Morley, S. K., Friedel, R. H. W., Cayton, T. E., & Noveroske, E. (2010). A rapid, global and prolonged electron radiation belt dropout observed with the Global Positioning System constellation. *Geophysical Research Letters,* 37, L06102. https://doi.org/10.1029/2010GL042772.

Ni, B., Bortnik, J., Thorne, R. M., Ma, Q., & Chen, L. (2013). Resonant scattering and resultant pitch angle evolution of relativistic electrons by plasmaspheric hiss. *Journal of Geophysical Research: Space Physics,* 118, 7740–7751. https://doi.org/10.1002/2013JA019260.

Nunn, D., 1993, A novel technique for the numerical simulation of hot collision-free plasma: Vlasov hybrid simulation, *J. Comput. Phys., 108,* 180-196.

Olifer, L., Mann, I. R., Morley, S. K., Ozeke, L. G., & Choi, D. (2018). On the role of last closed drift shell dynamics in driving fast losses and Van Allen radiation belt extinction. Journal of *Geophysical Research: Space Physics,* 123, 3692–3703. https://doi.org/10.1029/2018JA025190.

Onsager, T. G., Rostoker, G., Kim, H.-J., Reeves, G. D., Obara, T., Singer, H. J., & Smithtro, C. (2002). Radiation belt electron flux dropouts: Local time, radial, and particle-energy dependence. *Journal of Geophysical Research,* 107(A11), 1382. https://doi.org/10.1029/ 2001JA000187.

Paulikas, G. A. and Blake, J. B. (1979), Effects of the solar wind on magnetospheric dynamics: Energetic electrons at the synchronous orbit, in Quantitative Modeling of Magnetospheric Processes, edited by W. P. Olson, AGU, Washington, D. C., doi:10.1029/GM021p0180.

Pembroke, A., F. Toffoletto, S. Sazykin, M. Wiltberger, J. Lyon, V. Merkin, and P. Schmitt (2012), Initial results from a dynamic coupled magnetosphere-ionosphere-ring current model, *J. Geophys. Res.*, 117, A02211, doi:10.1029/2011JA016979.

Pham, K. H., W. Wang, B. Zhang, T. Dang, Huixin Liu, O. Brambles, K. Sorathia, J. Lei, V. Merkin, D. Lin, S. Bao, F. Toffoletto, A. Michael, J. Lyon, J. Garretson (2021), Thermospheric density enhancements produced by traveling atmospheric disturbances, *Geophys. Res. Lett.* https://doi.org/10.1002/essoar.10507693.1.

Reeves, G. D., K. L. McAdams, R. H. W. Friedel, and T. P. O'Brien (2003), Acceleration and loss of relativistic electrons during geomagnetic storms, *Geophys. Res. Lett.*, 30(10), 1529, doi:10.1029/2002GL016513.

Reeves, G. D., et al. (2011), On the relationship between relativistic electron flux and solar wind velocity: Paulikas and Blake revisited, *J. Geophys. Res.*, 116, A02213, doi:10.1029/2010JA015735.

Roederer, J. G. (1970), Dynamics of Geomagnetically Trapped Radiation, Cambridge Univ. Press, New York.

Shue, J.-H., et al. (1998), Magnetopause location under extreme solar wind conditions, *J. Geophys. Res.*, 103(A8), 17,691– 17,700, doi:10.1029/98JA01103.

Shen, X. ‐ C., Shi, Q., Wang, B., Zhang, H., Hudson, M. K., Nishimura, Y., et al. (2018), Dayside magnetospheric and ionospheric responses to a foreshock transient on 25 June 2008: 1. FLR observed by satellite and ground ‐ based magnetometers. *Journal of Geophysical Research: Space Physics*, 123. doi: 10.1029/2018JA025349.

Shprits, Y., Thorne, R., Friedel, R., Reeves, G., Fennell, J., Baker, D., & Kanekal, S. (2006). Outward radial diffusion driven by losses at magnetopause. *Journal of Geophysical Research*, *111*, A11214. https://doi.org/10.1029/2006JA011657.

Spence, H. E., et al. (2013), Science goals and overview of the Radiation Belt Storm Probes (RBSP) energetic particle, composition, and thermal plasma (ECT) Suite on NASA's Van Allen Probes mission. *Space Science Reviews*, 179, doi: 10.1007/s11214-013-0007-5.

Su, Z., Gao, Z., Zheng, H., Wang, Y., Wang, S., Spence, H. E., et al. (2017). Rapid loss of radiation belt relativistic electrons by EMIC waves. *Journal of Geophysical Research: Space Physics*, 122, 9880–9897. https://doi.org/10.1002/2017JA024169.

Summers, D., C. Ma, and T. Mukai (2004), Competition between acceleration and loss mechanisms of relativistic electrons during geomagnetic storms, *J. Geophys. Res.*, 109, A04221, doi:10.1029/2004JA010437.

Thorne, R.M., et al., 2013. Rapid local acceleration of relativistic radiation belt electrons by magnetospheric chorus. *Nature* 504, 7480. https://doi.org/10.1038/ nature12889..

Tsurutani, B. T. et al., 2006. Corotating solar wind streams and recurrent geomagnetic activity: A review*, J. Geophys. Res., 111*, A07S01, doi:10.1029/2005JA011273.

Tsyganenko, N.A., Sitnov, M.I., 2005. Modeling the dynamics of the inner magnetosphere during strong geomagnetic storms. *J. Geophys. Res.* 110, A03208. http://dx.doi.org/10.1029/2004JA010798.

Turner, D. L., Y. Y. Shprits, M. Hartinger, and V. Angelopoulos (2012a), Explaining sudden losses of outer radiation belt electrons during geomagnetic storms, *Nat. Phys.*, 8, 208– 212, doi:10.1038/NPHYS2185.

Turner, D. L., Angelopoulos, V., Li, W., Bortnik, J., Ni, B., Ma, Q., et al. (2014a). Competing source and loss mechanisms due to wave-particle interactions in Earth's outer radiation belt during the 30 September to 3 October 2012 geomagnetic storm. Journal of Geophysical Research: Space Physics, 119, 1960–1979. https://doi.org/10.1002/2014JA019770.

Turner, D. L., Angelopoulos, V., Morley, S. K., Henderson, M. G., Reeves, G. D., Li, W., et al. (2014b). On the cause and extent of outer radiation belt losses during the 30 September 2012 dropout event. *Journal of Geophysical Research: Space Physics,* 119, 1530–1540. https://doi.org/10.1002/2013JA019446.

Ukhorskiy, A. Y., Sitnov, M. I., Millan, R. M., Kress, B. T., Fennell, J. F., Claudepierre, S. G., & Barnes, R. J. (2015). Global storm time depletion of the outer electron belt. *Journal of Geophysical Research: Space Physics,* 120, 2543–2556. https://doi.org/10.1002/ 2014JA020645.

Wiltberger, M., et al. (2017), Effects of electrojet turbulence on a magnetosphere-ionosphere simulation of a geomagnetic storm, *J. Geophys. Res. Space Physics*, 122, 5008– 5027, doi:10.1002/2016JA023700.

Xiang, Z., Tu, W., Ni, B., Henderson, M. G., & Cao, X. (2018). A statistical survey of radiation belt dropouts observed by Van Allen Probes. *Geophysical Research Letters,* 45, 8035–8043. https://doi.org/10.1029/2018GL078907.

Yuan, C., and Q. Zong (2012), Quantitative aspects of variations of 1.5–6.0 MeV electrons in the outer radiation belt during magnetic storms, *J. Geophys. Res.*, 117, A11208, doi:10.1029/2011JA017346.

Zhang, B., Sorathia, K., Lyon, J., Merkin, V., Garretson, J. and Wiltberger, M. (2019), GAMERA: A Three-dimensional Finite-volume MHD Solver for Non-orthogonal Curvilinear Geometries, *The Astrophysical Journal Supplement Series*, 244, doi: 10.3847/1538-4365/ab3a4c.

Zong, Q., Rankin, R., & Zhou, X. (2017). The interaction of ultra-low-frequency Pc3-5 waves with charged particles in Earth's magnetosphere. *Reviews of Modern Plasma Physics,* 1, 10. https://doi.org/10.1007/s41614‐017‐0011‐4.

Zong, Q.-G., Zhou, X.-Z., Wang, Y. F., Li, X., Song, P., Baker, D. N., et al. (2009). Energetic electron response to ULF waves induced by interplanetary shocks in the outer radiation belt. Journal of Geophysical Research, 114, A10204. https://doi.org/10.1029/2009JA014393.

Figure 1. Differential electron flux vs. *L* value (vertical axis) and time (horizontal axis) from the Relativistic Electron Proton Telescope on Van Allen Probes (Baker et al., 2013) in three energy ranges from 1 January 2018 until the end of the mission. Arrows indicate the two event periods studied, a CME-shock event 13-14 May 2019 and a CIR event 30 Aug - 4 Sept 2019.

Figure 2. a) OMNIWeb solar wind data for 13 – 14 May 2019 CME-shock driven storm: speed Vsw, IMF Bz, density, pressure; Shue et al. (1998) magnetopause location and SymH in bottom two panels. CME-shock arrives at Earth ~ 00 UT 14 May. b) same for Aug-Sept 2019 CIR event. Vsw exceeds 600 km/s after 09 UT 31 Aug. The magnetopause location remains well outside geosynchronous for both events, however it is compressed inward to L = 8 for the CME-shock event. OMNIWeb time shift of L1 data to the noon bow shock is described at: https://omniweb.gsfc.nasa.gov/html/ow_data.html#time_shift

Figure 3. a) CME-shock simulation shown at 2200 UT 13 May 2019, using GAMERA 3D MHD code coupled to the Rice Convection Model and TIEGCM ionospheric model. Meridional plot of MHD pressure is shown on the right, with northern and southern hemispheric field aligned currents in the polar regions shown as inserts. On the left, residual Bz (dipole subtracted) is plotted along with an insert showing RCM pressure in the inner magnetosphere**.** Upstream solar wind input is taken from OMNIWeb (Figure 2) propagated to the 30 Re upstream boundary. b) Initial test particle populations in the GSM equatorial plane. Injected (red) and trapped (black) are the same for both May and Aug – Sept 2019 event studies prior to weighting with PSD measured from Van Allen Probes.

Figure 4. Radial profile of PSD for protons measured by REPT and MagEIS instruments on Van Allen Probe A for first invariant M = 2000 MeV/G (2 MeV at L = 6.6 in a dipole) and second invariant K =0.051 Re $G^{0.5}$ plotted vs. L* (Roederer, 1970) using the TS04D magnetic field model (Tsyganenko and Sitnov, 2005). Initial orbit is shown (blue) and subsequent orbits indicated over 48 hours from 0 UT 13 May (left) and 0 UT 29 Aug (right). Black curve is used for simulated initial PSD radial profile of the trapped population for each event.

Figure 5. Simulated PSD (trapped + injected) radial profile vs. L* following arrival of IP shock at L1 at 23:26 UT 13 May (http://wdc.kugi.kyoto-u.ac.jp/dst_realtime/201905/index.html) is shown. IMF Bz reaches a southward minimum 06 UT 14 May and min Dst = -65 nT at 08 UT, see Fig. 2a. The blue patch of low PSD in the upper left corner is due to mapping from L to L* since test particles are initialized inside L = 6 Re, see Figure 3b, which is inside L* = 6 Re using the TS04D magnetic field model for mapping.

Figure 6. Simulated PSD (trapped + injected) radial profile vs. L* using TS04 model during the CIR interval shown in Fig. 2b. Vsw exceeds 600 km/s after 09 UT 31 Aug, IMF Bz is oscillatory around 0 nT with min Dst = - 52 nT at 07 UT on 1 Sept in Fig. 1b. Test particle simulation was started at 00 UT 30 Aug and ran until 0900 UT on 2 Sept.

Figure 7. Comparison of simulated PSD radial profile at the end of the time intervals shown in Figures 5 and 6 (black dots) with measured PSD profiles from Van Allen Probes over sequential orbits. Initial orbit is shown (blue) and subsequent orbits are indicated over 48 hours from 0 UT 13 May (top) and 0 UT 30 Aug (bottom). Black dots indicate end of the simulation (after 34 hours of data shown for the May event and at 0 UT on 3 Sept for the September event) using PSD updated at apogee every 9 hours for the RBSPA and RBSP B spacecraft as available, with data combined for the May event and only RBSP A measurements available every 9 hours for the September event. bbb